Scientific Research Publishing

Journal of Materials Science and Chemical Engineering, 2026, 14(2), 15-34
https://www.scirp.org/journal/msce
ISSN Online: 2327-6053
ISSN Print: 2327-6045

# 3D Electrospinning of Pd/TiO₂-Based Nanofibrous Aerogel Catalysts for Catalytic Infrared Heating

**Qiying Zhao[1], Qunhui Jiang[2], Wenjuan Qu[1], Haile Ma[1*], Jianwei Lu[3*]**

[1]School of Food and Biological Engineering, Jiangsu University, Zhenjiang, China
[2]Zhenjiang Meibo Infrared Technology Co., Ltd., Zhenjiang, China
[3]School of Materials Science and Engineering, Jiangsu University, Zhenjiang, China
Email: zqytxq@163.com, *mhl@ujs.edu.cn

**How to cite this paper:** Zhao, Q.Y., Jiang, Q.H., Qu, W.J., Ma, H.L. and Lu, J.W. (2026) 3D Electrospinning of Pd/TiO₂-Based Nanofibrous Aerogel Catalysts for Catalytic Infrared Heating. *Journal of Materials Science and Chemical Engineering*, **14**, 15-34.
https://doi.org/10.4236/msce.2026.142002

**Received:** January 10, 2026
**Accepted:** February 6, 2026
**Published:** February 9, 2026

## Abstract

Catalytic infrared heating offers an energy-efficient and low-emission alternative to traditional flame-based heating. However, its practical application is limited by the insufficient activity, thermal durability, and structural stability of current catalysts under continuous combustion conditions. In this study, Pd-doped $TiO_2/SiO_2/Y_2O_3$ nanofibrous aerogel catalysts (PTSY-NFAs) with tunable Pd loadings were synthesized via a one-step 3D sol-gel electrospinning technique, followed by calcination. This process resulted in a binder-free, continuously interconnected nanofibrous aerogel framework characterized by high surface area, excellent thermal stability, and strong mechanical resilience. The influence of Pd loading on the microstructure, redox behavior, and catalytic performance was examined systematically. The optimized PTSY-11-NFA catalyst achieved an LPG conversion efficiency of 99% and a peak infrared surface temperature of 587˚C. A prototype catalytic infrared heater integrated with this catalyst displayed uniform surface temperatures ranging from 423˚C to 509˚C and maintained stable long-term operation, surpassing the performance of a commercial catalyst. This study demonstrates a scalable design strategy for noble metal-doped ceramic nanofibrous aerogels aimed at achieving high-efficiency catalytic infrared heating.

## Keywords

3D Electrospinning, Nanofibrous Aerogel, Catalytic Infrared Heating, Catalytic Combustion

## 1. Introduction

Against the backdrop of increasingly stringent requirements for low-carbon development and efficient energy utilization, catalytic infrared heating has emerged as an efficient and environmentally benign energy conversion technology that directly transforms the chemical energy of fossil fuels into infrared radiant heat [1]-[3]. Compared to traditional flame-based heating, catalytic infrared heating offers higher energy efficiency, significantly reduced emissions of CO and $NO_x$, and improved heating uniformity. This makes it particularly appealing for applications in food processing, industrial coating curing, waste gas treatment, and residential heating systems [4]-[7]. Catalytic infrared heating involves the complete oxidation of hydrocarbon fuels on preheated catalyst surfaces, producing $CO_2$ and $H_2O$ while simultaneously generating infrared radiant heat [8] [9]. Therefore, the catalytic activity, thermal stability, and structural properties of the catalyst are crucial in determining both infrared radiative performance and long-term operational stability. Designing catalysts that combine high catalytic activity with robust durability remains a significant challenge for large-scale deployment of this technology.

Given the critical importance of catalyst properties, Pd and Pt-based noble metal catalysts supported on ceramic fibers, metallic substrates, or carbonaceous materials are currently the predominant choice for catalytic infrared heaters [10] [11]. The exceptional catalytic activity of Pd and Pt toward hydrocarbon oxidation is dictated not only by the dispersion and valence states of the noble metals but also by the physicochemical attributes of the supports, such as specific surface area, pore architecture, and thermal stability [12] [13]. Among various support materials, ceramic nanofibers—including $TiO_2$, $SiO_2$, $Al_2O_3$, and their composites—are particularly promising due to their high surface area, mechanical robustness, and superior thermal stability [14]-[16]. In particular, nanofibrous ceramic aerogels (NFAs), an emerging class of ultralight, three-dimensional porous materials, have garnered significant attention. By combining the high surface area of nanofibers with the continuously interconnected porous network of aerogels, NFAs host noble metal nanoparticles to provide abundant stable active sites, thereby enhancing catalytic efficiency [17] [18]. Moreover, their intrinsic flexibility and structural integrity enable direct integration into catalytic infrared heaters with complex geometries, offering clear advantages in mechanical stability and structural compatibility over conventional powder-based or bulk catalyst systems [19] [20].

The fabrication of ceramic nanofibers is well established via the combination of electrospinning and sol-gel techniques, allowing for precise control over fiber morphology through the tuning of spinning parameters [21] [22]. Historically, the construction of 3D nanofibrous aerogels relied on multi-step reconstruction strategies, such as the fiber-cutting, slurry-preparation, and freeze-drying approach pioneered by Ding and co-workers [23]-[25]. While these methods yield low-density materials, they typically necessitate binders to form a network. Consequently, the lack of robust physical entanglement and chemical bonding often compromises structural integrity, particularly under the harsh conditions of prolonged thermal cycling or high-velocity gas flow required for catalytic heating [26]. To overcome these intrinsic limitations, the field has witnessed a paradigm shift toward one-step 3D electrospinning. This scalable strategy eliminates the need for post-processing steps like fiber cutting. By judiciously tailoring the solution rheology, fibers spontaneously assemble into a continuous, ultralight, and binder-free network during deposition [27] [28]. Recent studies have validated the efficacy of this approach, Zhang *et al.* [29] utilized 3D electrospinning to construct hierarchically porous aerogels with high elasticity, while Li *et al.* [30] further demonstrated the technique's versatility by developing structurally tunable aerogels with excellent energy absorption. These advancements, which preserve inter-fiber connectivity and enhance mechanical resilience, offer a promising pathway for developing advanced nanofibrous aerogels specifically tailored for catalytic infrared heating applications.

In this study, Pd-doped $TiO_2/SiO_2/Y_2O_3$ nanofibrous aerogel catalysts (PTSY-NFAs) with varying Pd loadings (2, 5, 8, and 11 mol%) were synthesized via a one-step 3D sol-gel electrospinning process followed by calcination at 600˚C. The effect of Pd loading on the microstructural evolution, textural characteristics, and catalytic behavior of the resulting aerogels was systematically investigated. Particular emphasis was placed on evaluating the catalytic activity, infrared radiative performance, and long-term operational stability during LPG combustion. Furthermore, a prototype catalytic infrared heater was assembled using the optimized PTSY-NFA catalyst to assess its practical feasibility and heating performance under realistic operating conditions.

## 2. Experimental Materials and Methods

### 2.1. Materials

Polyvinylpyrrolidone (PVP, MW = 1300000), Titanium (IV) isopropoxide (TIP, 95%), Tetraethoxysilane, absolute ethanol (99.5%), Yttrium nitrate hexahydrate ($Y(NO_3)_3 \cdot 6H_2O$), and Palladium acetate (Pd 46% - 48%) were all purchased from Aladdin Chemical Co., Ltd., China. Liquefied petroleum gas (LPG) was purchased from Jiangsu Huada Gas Co., Ltd., China. Commercial catalyst ($Pd/Al_2O_3$ glass fiber cotton) was purchased from Shanghai Macklin Biochemical Co., Ltd., China. All the initial chemicals were used without further purification.

### 2.2. Preparation of Catalysts

The preparation of 3D nanofibrous aerogel catalysts involves several steps, as shown in **Figure 1**. First, a pale yellow precursor solution of $TiO_2/SiO_2/Y_2O_3$ (TSY) was prepared following the protocol reported by Dong *et al.* [26]. The molar ratio of Ti: Si: Y was fixed at 1:1:0.11. Subsequently, varying amounts of palladium acetate were incorporated into this solution. The molar ratios of Pd to the combined Ti and Pd content were adjusted to 2%, 5%, 8%, and 11%, corresponding to the samples PTSY-2, PTSY-5, PTSY-8, and PTSY-11, respectively. This procedure yielded a series of black spinning solutions.

The electrospinning process was carried out using a DP-30 spinning apparatus. The solution was delivered through a 19G needle at a flow rate of 5 mL/h, with the nozzle-to-collector distance maintained at 15 cm. A high voltage of 25 kV (Genvolt High Voltage Power Supply) was applied. The ambient temperature and humidity were 21˚C ± 2˚C and 45% ± 15%, respectively, without additional control. Under these conditions, 3D nanofibrous aerogels could be reproducibly fabricated. The nanofibers were collected on a grounded copper plate. The as-spun nanoceramic fibers were subsequently calcined in a muffle furnace, heated to 600˚C at a rate of 5˚C/min in air, maintained at this temperature for 2 h, and then allowed to cool naturally to room temperature. Based on the precursor spinning solutions, the resulting nanoceramic nanofibrous aerogels were designated TSY-NFAs, PTSY-2-NFAs, PTSY-5-NFAs, PTSY-8-NFAs, and PTSY-11-NFAs, respectively.

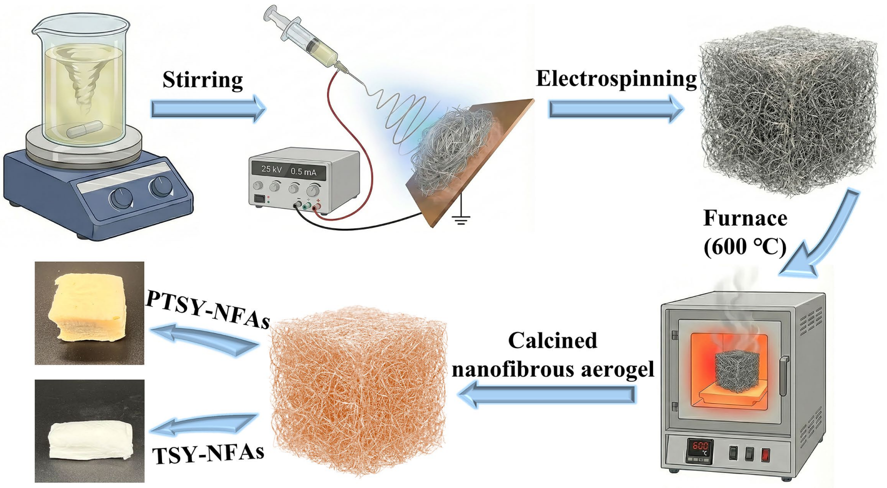

**Figure 1.** Flow chart of the electrospinning preparation of the catalyst.

## 2.3. Catalyst Characterization

The morphology and structure of the catalyst were analyzed using a high-resolution transmission electron microscope (HRTEM, JEM-2100F) (JEOL, Tokyo, Japan). Statistical distributions of the fiber diameters were calculated by measuring 50 distinct fibers (N = 50) using ImageJ software. The crystal structure of the catalyst was determined by X-ray diffraction (XRD, Rigaku D-Max/RB, Tokyo, Japan). X-ray photoelectron spectroscopy (XPS) was used to analyze the surface species of the catalyst on a Kratos XSAM800 spectrometer (Shimadzu/Kratos, Manchester, UK) with Al Kα ($h\nu = 1486.6$ eV) X-rays. The thermal stability of the catalyst was analyzed using a TMA-402-F3 thermogravimetric analyzer (NETZSCH, Germany). The functional groups of the catalyst were analyzed using an is50 Fourier transform infrared spectrometer (Thermo Fisher Scientific, USA). The specific surface area and pore structure of the catalyst were analyzed using an Autosorb iO chemisorption analyzer (Quantachrome Instruments, USA). The mechanical properties of the catalyst were measured using a CMT6130 universal electronic testing machine. The reducibility of the catalyst was analyzed using an AutoChem II 2920 temperature-programmed chemisorption analyzer (Micromeritics, USA).

### 2.4. Catalytic Combustion Performance Test

The catalytic infrared combustion performance of the aerogel catalysts toward LPG was evaluated using a laboratory-built micro-scale catalytic combustion system, as schematically illustrated in **Figure 2**. For each test, a catalyst sample (approximately 50 mg, shaped into a 20 mm × 20 mm × 10 mm cuboid) was positioned within the combustion chamber of a quartz tube (inner diameter: 50 mm). LPG was employed as the fuel gas at a constant flow rate of 27 mL/min, controlled by an LZB-3WB flowmeter (Taizhou Junhai Instrument Co., Ltd.), while the air flow rate was regulated between 0.3 and 1.5 L/min. The surface temperature of the catalyst during combustion was continuously monitored using a thermocouple. This range corresponds to an excess air coefficient ($\lambda$) spanning from 0.5 (fuel-rich) to 2.3 (fuel-lean), effectively simulating the transition from startup to steady-state industrial operation. To ensure steady-state conditions, the system was equilibrated for 10 min at each testing condition prior to data recording. Simultaneously, the real-time variation in exhaust gas composition was analyzed under ambient pressure using a QB10N intelligent gas detection sensor (Henan Chicheng Electric Co., Ltd.). Consequently, the catalytic performance was assessed based on both the combustion temperature and LPG conversion efficiency. The LPG conversion ($X_{LPG}$, %) was calculated according to Equation (1).

$$X_{LPG} = \frac{\varphi_{LPG,in} - \varphi_{LPG,out}}{\varphi_{LPG,in}} \times 100\% \quad (1)$$

In the equation presented above, $\varphi_{LPG,in}$ refers to the volume fraction of liquefied petroleum gas before the reaction, %; $\varphi_{LPG,out}$ refers to the volume fraction of liquefied petroleum gas after the reaction, %.

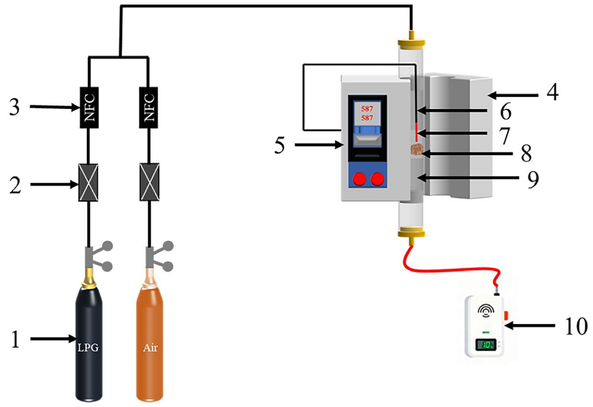

**Figure 2.** Schematic diagram of the experimental system for catalytic infrared combustion: Gas cylinder (1); Check valve (2); Gas mass flow meter (3); Electric heating furnace (4); Temperature controller (5); Thermocouple compensation cable (6); Type K thermocouple (7); Catalyst (8); Quartz catalytic bed (9); Intelligent gas detection sensor (10).

### 2.5. Preparation and Testing of Small Infrared Heaters

The nanofibrous aerogel exhibiting the optimal catalytic performance was selected to fabricate a prototype catalytic infrared heater with dimensions of 20 cm × 15 cm × 15 cm. Figure 3 presents the photograph, schematic diagram, and internal configuration of the heater. The operating principle relies on the supply of LPG, which undergoes flameless combustion upon contact with the preheated catalyst surface. As shown in Figures 3(c) and Figures 3(d), this process generates $CO_2$ and $H_2O$ while simultaneously releasing energy in the form of infrared radiant heat. Subsequently, the surface temperature distribution of the heater was evaluated.

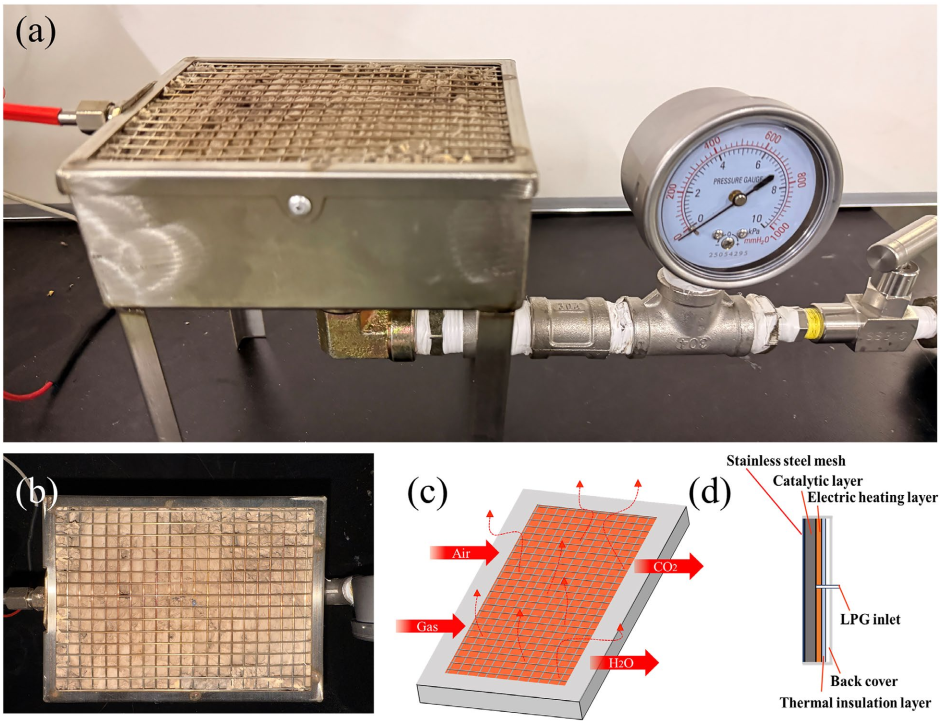

**Figure 3.** Structure of the catalytic infrared heater: (a) and (b) Physical diagrams of the catalytic infrared heater; (c) Schematic diagrams of the planar model and reaction process of the heater; (d) Schematic diagram of the internal structure of the heater.

## 3. Results and Discussion

### 3.1. Structural Properties of Catalysts

#### 3.1.1. Surface Morphology Analysis of Catalyst

The morphology of nanofibrous aerogel catalysts is pivotal in determining both their mechanical integrity and catalytic performance during combustion. As shown in Figure 4(a), the as-spun TSY-NFAs exhibited a continuous and well-interconnected nanofibrous network with an average fiber diameter of approximately 1418 nm, as calculated from the corresponding diameter distribution histogram (Figure 4(b)). In contrast to conventional multi-step strategies relying on binder-bonded short fibers, this one-step technique generates a physically entangled, binder-free framework, thereby eliminating binder-induced structural weaknesses. Following calcination at 600˚C, the integral fibrous architecture was well preserved (**Figure 4(c)**), avoiding the skeletal collapse or pore blockage typical of binder-based aerogels upon organic decomposition. Notably, the average fiber diameter decreased to 908 nm (**Figure 4(d)**); this reduction is primarily attributed to the decomposition of organic components and the subsequent volume contraction of the ceramic fibers during thermal treatment.

The morphology of the Pd-doped nanofibrous aerogels was further scrutinized at varying magnifications. As shown in **Figure 4(e)**, the PTSY-11-NFAs exhibited a highly porous architecture characterized by isotropically distributed, open macroscopic pores, a feature conducive to efficient gas diffusion and the catalytic combustion of LPG. The highlighted regions in **Figure 4(f)** underscore the continuous nature of individual nanofibers, corroborating the integrity of the three-dimensional fibrous network following Pd incorporation. High-magnification SEM images (**Figure 4(g)**) revealed that the nanofibers retained smooth surfaces and relatively uniform diameters, averaging approximately 985 nm (**Figure 4(h)**). These observations confirm that Pd doping did not compromise the nanofibrous aerogel framework, thereby maintaining the structural attributes pivotal for both mechanical stability and catalytic performance.

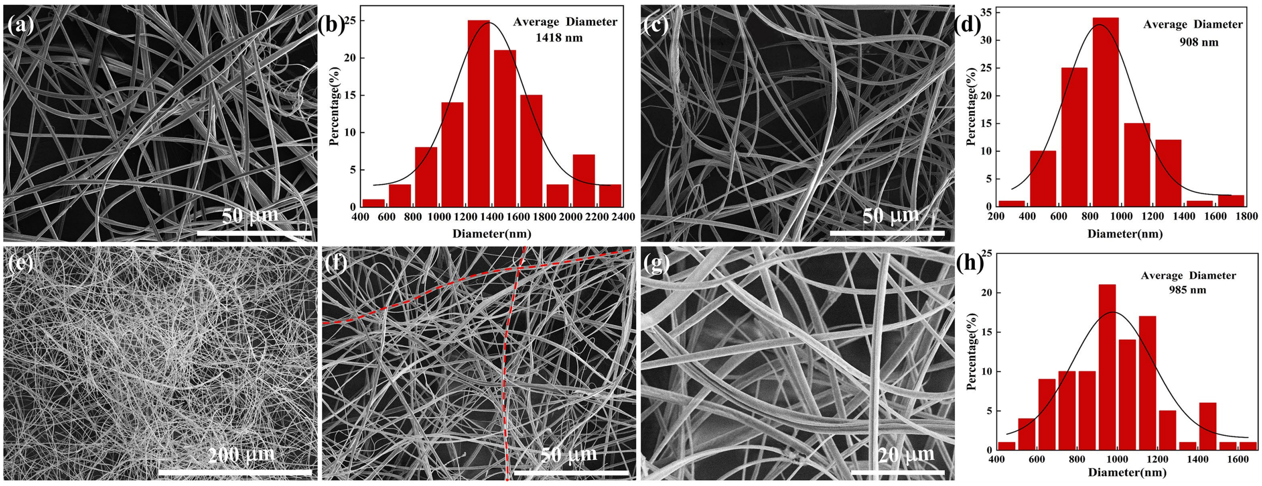

**Figure 4.** Microstructure diagrams of different nanofibrous aerogels. (a)-(d) SEM images of TSY-NFAs before and after calcination, with histograms of the diameter distribution of TSY-NFAs before and after calcination; (e)-(f) SEM images of PTSY-11-NFAs at different magnifications; (h) Histogram of the diameter distribution of PTSY-11-NFAs.

### 3.1.2. Thermal Stability Analysis of Catalyst

The thermal decomposition characteristics of the precursor fibers were analyzed to guide the ceramicization process. As shown in **Figures 5(a)** and **Figures 5(b)**, the TG curves of PVP/TSY-NFAs and PVP/PTSY-11-NFAs exhibited similar thermal decomposition profiles. Both samples experienced a distinct two-stage weight-loss process. Initially, a mass loss of approximately 16.4% occurred from room temperature to 200˚C, attributed to the evaporation of physically adsorbed moisture and residual organic solvents. The second, more pronounced weight loss took place between 200˚C and 500˚C. This stage corresponded to the decomposition of the PVP polymer backbone and the removal of residual organics, resulting in a mass loss of approximately 29.6%. Above 600˚C, negligible weight loss was observed, indicating the complete removal of organic components and the formation of a stable inorganic framework. Consequently, both calcined TSY-NFAs and PTSY-11-NFAs demonstrated excellent thermal stability. This confirms that Pd incorporation does not compromise the structural integrity of the catalysts under high-temperature conditions.

To further clarify the chemical evolution of the polymeric components during calcination, the FTIR spectra of TSY-NFAs and PTSY-11-NFAs treated at varying temperatures were analyzed (Figure 5(c) and Figure 5(d)). At lower calcination temperatures, both samples exhibited similar characteristic absorption bands, suggesting comparable decomposition behaviors. The absorption peaks located at approximately 1650, 1540, 1425, and 1291 cm$^{-1}$ are ascribed to the vibrational modes of PVP, corresponding to C=O, $C(=O)\ O^-$, $-CH_2$, and C-N groups, respectively. As the calcination temperature increased, the intensities of these organic-related peaks progressively diminished, eventually becoming negligible at 600˚C. This observation confirms the near-complete decomposition of the PVP matrix. These findings corroborate the TG results, collectively verifying the effective removal of polymeric species and the subsequent formation of a stable inorganic aerogel framework.

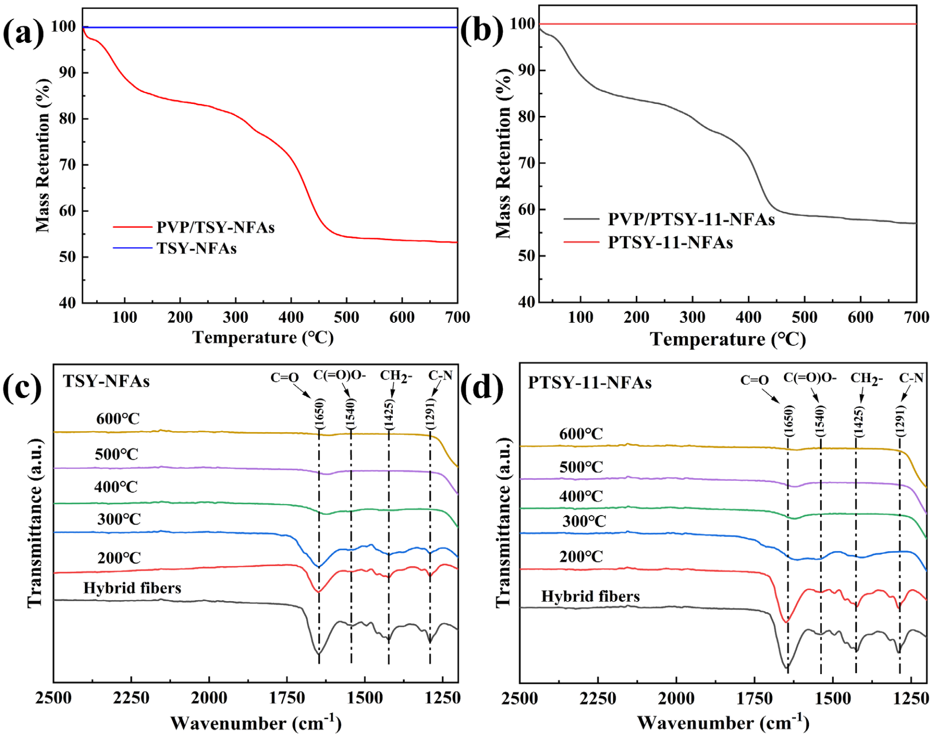

**Figure 5.** (a) TG curves of PVP/TSY-NFAs and TSY-NFAs; (b) TG curves of PVP/PTSY-11-NFAs and PTSY-11-NFAs; (c) FTIR spectra of TSY-NFAs and (d) PTSY-11-NFAs at different calcination stages.

### 3.1.3. Chemical State and Crystal Structure Analysis of Catalysts

According to related studies, the crystal structure and valence states of active metal species play a decisive role in determining catalytic performance [31] [32]. To clarify the crystalline phases and chemical states of Pd in the synthesized nanofibrous aerogel catalysts, XRD and XPS analyses were systematically conducted, as summarized in **Figure 6**. The XRD patterns of TSY-NFAs and Pd-doped PTSY-NFAs with different Pd loadings are presented in **Figure 6(a)**. All samples exhibit a broad diffraction peak centered at $2\theta = 23^\circ$, characteristic of amorphous $SiO_2$. In addition, a broadened diffraction peak located at $2\theta = 25.3^\circ$ is assigned to the (101) plane of anatase $TiO_2$. The pronounced peak broadening suggests reduced crystallinity, which can be attributed to lattice distortion induced by the incorporation of amorphous $SiO_2$ into the $TiO_2$ lattice [33] [34]. With increasing Pd loading, distinct diffraction peaks emerge at $2\theta = 33.9^\circ$, $41.9^\circ$, and $54.7^\circ$ in the PTSY-11-NFAs, corresponding to the (101), (110), and (112) crystal planes of PdO, respectively. Notably, the anatase $TiO_2$ diffraction peak in PTSY-11-NFAs becomes sharper compared with that of TSY-NFAs, indicating that Pd incorporation effectively alleviates lattice distortion and enhances the crystallinity of anatase $TiO_2$. The relatively narrow and intense PdO peaks further suggest good crystallinity of the PdO phase within the nanofibrous aerogel matrix.

The surface elemental composition and chemical states of the Pd-doped nanofibrous aerogels were investigated via XPS analysis. As shown in the survey spectra (**Figure 6(b)**), all Pd-containing samples exhibited distinct signals for O, Ti, Si, Y, and Pd, corroborating the successful incorporation of Pd into the aerogel framework. The detection of a carbon signal is attributed to the partial carbonization of PVP during calcination, a phenomenon frequently observed in sol-gel derived oxide systems [35]. To identify the valence states of palladium, the high-resolution Pd 3d spectra (**Figure 6(c)**) were deconvoluted into two pairs of spin-orbit doublets. The peaks located at binding energies of approximately 336.9 eV (Pd $3d_{5/2}$) and 342.2 eV (Pd $3d_{3/2}$) are assigned to $Pd^{2+}$ species, while those at around 335.0 eV and 340.2 eV correspond to metallic $Pd^0$ [36]. The coexistence of $Pd^{2+}$ and $Pd^0$ indicates partial reduction of $Pd^{2+}$ during calcination at elevated temperatures, which is commonly observed in $Pd/TiO_2$ systems owing to strong metal-support interactions [37]. The binding energy ranges observed for $Pd^{2+}$ (Pd $3d_{5/2}$: 336 - 340 eV; Pd $3d_{3/2}$: 341 - 345 eV) align well with literature values [38], confirming that Pd in the nanofibrous aerogel predominantly exists as $Pd^{2+}$ species, with a minor fraction of metallic $Pd^0$. The coexistence of these Pd species is beneficial for redox cycling and oxygen activation during catalytic combustion, thereby enhancing catalytic performance [39].

The elemental distribution within the nanofibrous aerogels was further scrutinized via EDS mapping of a representative PTSY-11-NFA nanofiber (**Figures 6(d)-(i)**). The mapping results revealed a smooth and continuous morphology, characterized by the uniform distribution of Ti, O, and Si throughout the fiber matrix. Notably, Pd was homogeneously dispersed along the nanofiber devoid of discernible agglomeration, while Y, despite its lower concentration, also exhibited uniform distribution. These observations corroborate the XPS results, verifying the successful integration of all components into the aerogel framework. While a direct comparison with Y-free samples was not conducted in this study, previous literature suggests that Yttrium species can effectively inhibit grain growth and suppress phase transformation in zirconia and titania-based systems [40]. Therefore, it is hypothesized that the uniform distribution of Y in the current PTSY system likely contributes to maintaining the structural integrity of the nanofibrous network during high-temperature calcination.

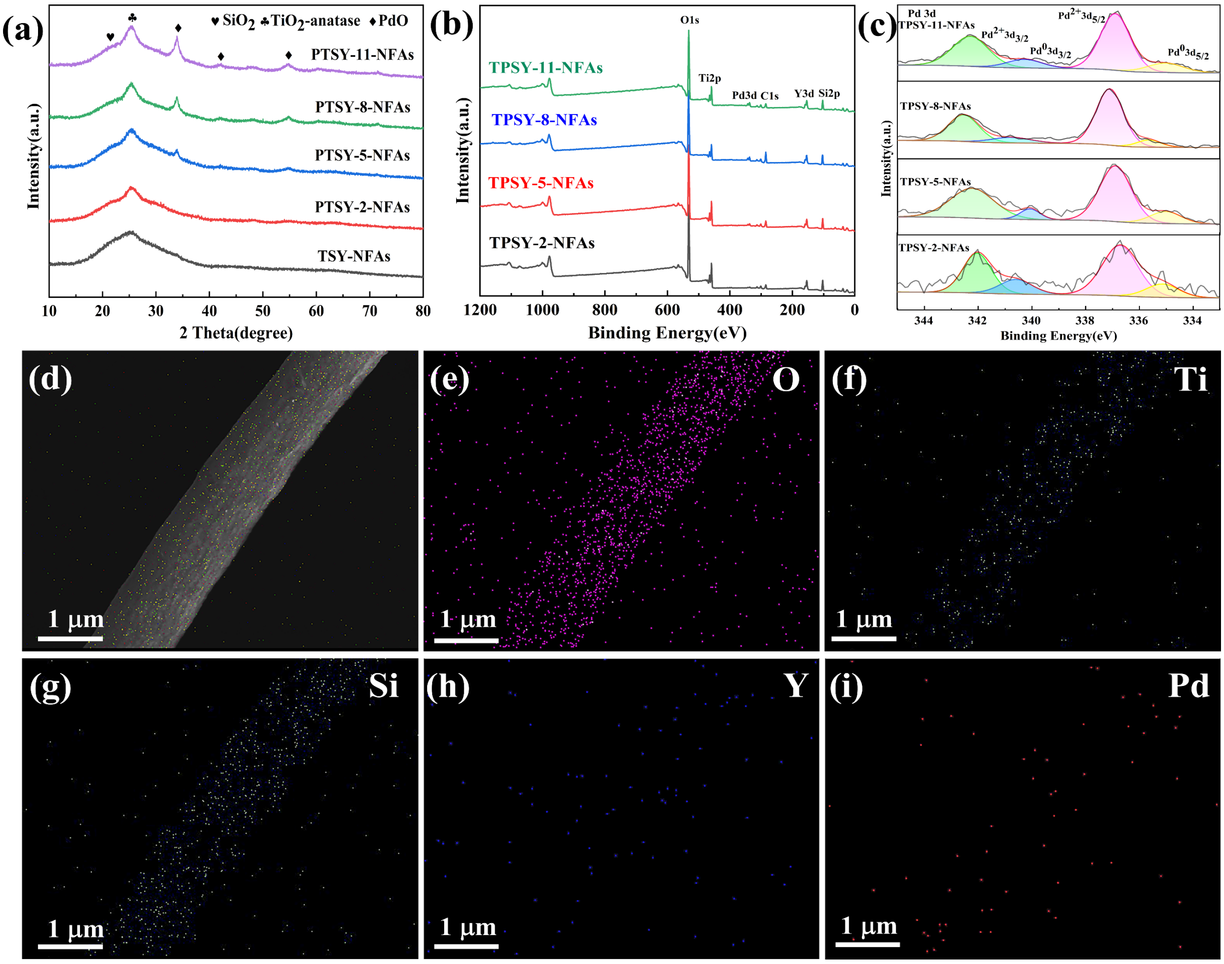

**Figure 6.** (a) XRD spectra of TSY-NFAs, PTSY-2-NFAs, PTSY-5-NFAs, PTSY-8-NFAs, and PTSY-11-NFAs. (b)-(c) XPS survey spectra and Pd 3d XPS spectra of PTSY-2-NFAs, PTSY-5-NFAs, PTSY-8-NFAs, and PTSY-11-NFAs; (d)-(i) EDS elemental mapping image of PTSY-11-NFAs.

### 3.1.4. Mechanical Property Analysis of Catalysts

Mechanical characterization was conducted to assess the structural robustness and elasticity of the TSY-NFAs. As shown in Figure 7(a), the compressive stress-strain ($\sigma$-$\varepsilon$) curves of TSY-NFAs exhibited a robust quasi-linear elastic response up to 60% strain with negligible plastic deformation. This remarkable elasticity is critical for heater assembly; it allows the catalyst to be slightly pre-compressed into the reactor housing, ensuring conformal contact with the walls. This tight packing effectively eliminates edge voids, preventing gas channeling and forcing the fuel-air mixture to permeate uniformly through the mesoporous network for maximum catalytic utilization. Furthermore, the long-term structural integrity under dynamic conditions was assessed via cyclic compression tests (Figure 7(b)). The aerogels retained over 90% of their maximum stress with minimal permanent deformation of only 6%. In a practical combustion environment, the heater undergoes repeated thermal expansion and contraction. The demonstrated fatigue resistance suggests that the PTSY-NFA catalyst can act as a "mechanical cushion," accommodating thermal stresses and operational vibrations without pulverization or settling. The energy dissipation coefficient, calculated to be as low as 0.22 in the first cycle (Figure 7(c)), further indicates efficient elastic recovery rather than energy absorption through damage accumulation.

A macroscopic test (Figure 7(d)) visually corroborated this resilience, showing rapid recovery after substantial loading. Finally, comparative analysis (Figure 7(e) and Figure 7(f)) confirmed that increasing Pd loading to 11 mol% caused negligible fluctuations in the compressive modulus and energy dissipation (maintained at 0.25). This confirms that the active metal phase does not compromise the elasticity of the support, ensuring that the optimized catalytic sites are housed within a mechanically stable framework capable of sustaining uniform combustion over extended operational periods.

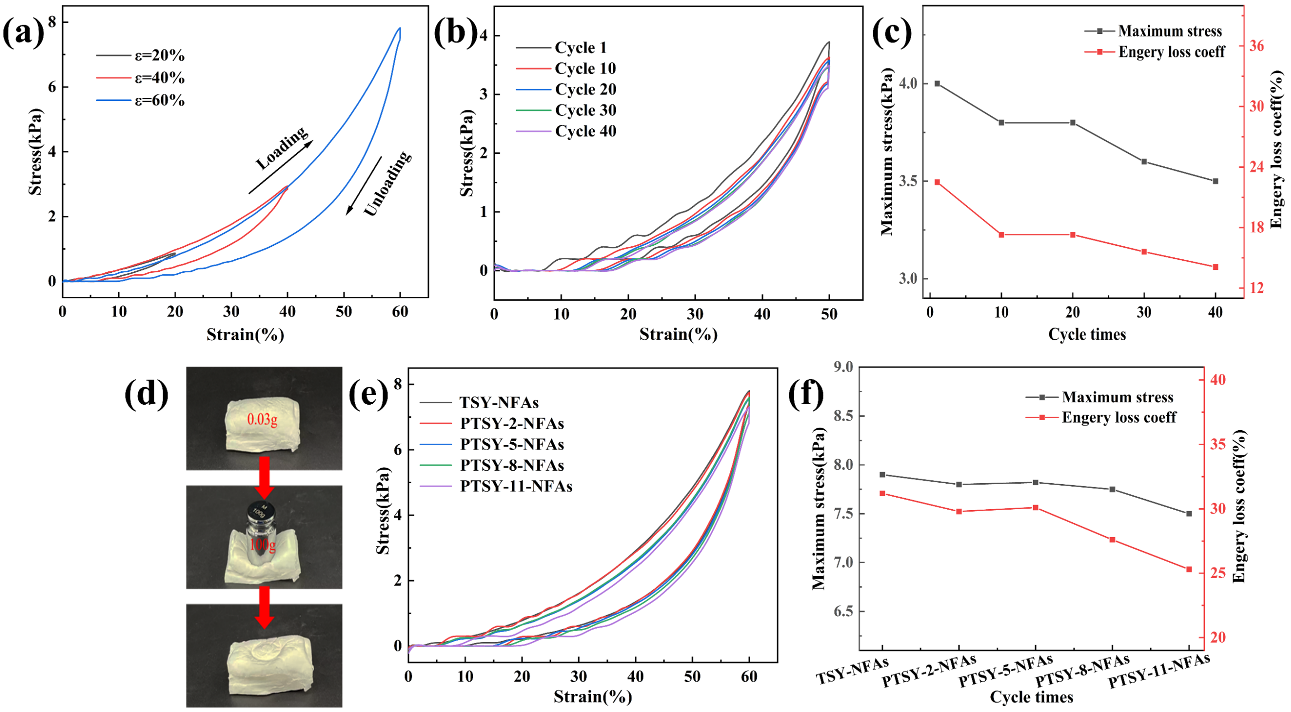

Figure 7. (a) Compressive $\sigma$-$\epsilon$ curves of TSY-NFAs under different strains of 20%, 40%, and 60%; (b) 40-cycle fatigue compression tests of TSY-NFAs at $\varepsilon = 50\%$; (c) Variations of maximum stress and energy loss coefficient with the number of compression cycles; (d) TSY-NFAs can quickly recover from large compressive deformation; (e) Compressive $\sigma$-$\epsilon$ curves of TSY-NFAs, PTSY-2-NFAs, PTSY-5-NFAs, PTSY-8-NFAs, and PTSY-11-NFAs at $\varepsilon = 60\%$; (f) Maximum stress and energy loss coefficients of TSY-NFAs, PTSY-2-NFAs, PTSY-5-NFAs, PTSY-8-NFAs, and PTSY-11-NFAs.

### 3.1.5. Texture Properties Analysis of Catalysts

The specific surface area and pore architecture are pivotal factors governing the catalytic performance of nanofibrous aerogels. As displayed in **Figure 8**, the $N_2$ adsorption-desorption isotherms of all prepared samples exhibited Type IV curves with $H_2$-type hysteresis loops. According to IUPAC classification, these features indicate the presence of distinct mesoporous structures within the aerogels [41]. Notably, increasing the Pd loading from 0 to 11 mol% resulted in a gradual increase in both the specific surface area and the average pore size (**Table 1**). This enhancement is primarily attributed to the suppression of lattice distortion in anatase $TiO_2$ by Pd doping, which stabilizes the crystal structure. Such stability facilitates gas diffusion during LPG combustion, thereby contributing to the observed improvement in catalytic activity.

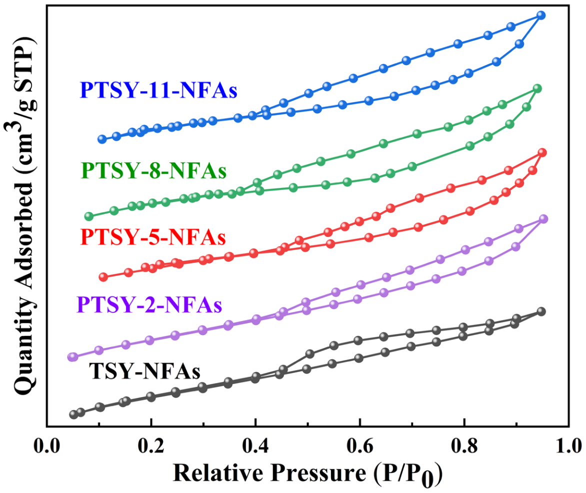

**Figure 8.** $N_2$ adsorption-desorption isotherms of TSY-NFAs, PTSY-2-NFAs, PTSY-5-NFAs, PTSY-8-NFAs, and PTSY-11-NFAs nanofibrous aerogels.

**Table 1.** Texture properties of TSY-NFAs, PTSY-2-NFAs, PTSY-5-NFAs, PTSY-8-NFAs, and PTSY-11-NFAs nanofibrous aerogels.

| Nanofibrous aerogels | Specific surface area/($m^2 \cdot g^{-1}$) | total pore volume /($cm^3 \cdot g^{-1}$) | average pore size/nm |
|---|---|---|---|
| TSY-NFAs | 78.8 | 0.023 | 4.11 |
| PTSY-2-NFAs | 85.6 | 0.035 | 5.59 |
| PTSY-5-NFAs | 90.3 | 0.041 | 6.87 |
| PTSY-8-NFAs | 96.8 | 0.059 | 8.96 |
| PTSY-11-NFAs | 100.7 | 0.077 | 10.12 |

### 3.1.6. Reduction Analysis of Catalysts

The reduction behavior of the PTSY-NFA series was systematically investigated via $H_2$-TPR analysis (**Figure 9**). Crucially, the reduction profiles offer direct insights into the availability of active oxygen species required for the catalytic oxidation of LPG. All catalysts exhibited a negative peak in the temperature range of 65˚C - 75˚C. This inverted signal is widely identified as the thermal decomposition of palladium hydride ($PdH_X$) [42]. As the Pd loading increased, this peak became more pronounced, indicating stronger Pd-H interactions and the progressive nucleation of Pd particles within the nanofibrous framework. Such structural evolution facilitates PdO reduction. Furthermore, it promotes the reversible transformation between $Pd^0$ and $Pd^{2+}$ during catalytic cycles [36].

For PTSY-5, PTSY-8, and PTSY-11-NFAs, an additional reduction peak emerged near 105˚C. This feature corresponds to the reduction of PdO species with weak metal-support interactions. Notably, PTSY-11-NFAs exhibited a distinct secondary peak at 178˚C. This signal is attributed to the reduction of highly dispersed PdO clusters that remained unreduced at lower temperatures. Such behavior suggests that higher Pd loading induces structural heterogeneity. Specifically, smaller PdO domains exhibit stronger metal-support interactions, thereby necessitating higher energy for reduction [37].

Additionally, all catalysts exhibited a weak, broad reduction signal between 450˚C and 500˚C. This feature is attributed to the surface reduction of Ti4+ species within the $TiO_2$ matrix [43], which contributes negligibly to the overall catalytic performance. In contrast, distinct high-temperature reduction peaks near 670˚C were observed for the samples with lower Pd loadings (PTSY-2 to PTSY-8). These peaks arise from strong interfacial interactions between PdO and the $TiO_x/SiO_x$ support, rendering them difficult to reduce and thus catalytically inert at typical operating temperatures. The complete absence of this high-temperature signal in PTSY-11-NFAs indicates that the optimized Pd loading prevents the formation of these "locked" inactive species. Consequently, the superior reducibility of PTSY-11-NFAs ensures that a maximal fraction of palladium active sites remains available for the redox reaction, validating its superior catalytic combustion performance.

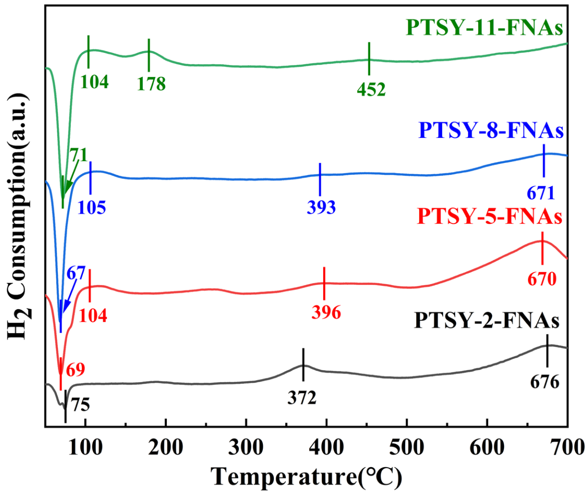

**Figure 9.** $H_2$-TPR curves of PTSY-2-NFAs, PTSY-5-NFAs, PTSY-8-NFAs, and PTSY-11-NFAs.

## 3.2. Catalytic Performance Assessment of Catalysts

The LPG conversion efficiency and catalytic infrared temperature of the aerogel series were initially evaluated under varying air flow rates (**Figure 10(a)** and **Figure 10(b)**). As shown in **Figure 10(a)**, the LPG conversion efficiency increased progressively with the air flow rate. Notably, PTSY-11-NFAs achieved a maximum conversion of 99% at 0.7 L/min. This superior performance is ascribed to the synergistic effects of high Pd loading, large specific surface area, and enriched surface lattice oxygen. These factors collectively promote active oxygen mobility and enhance catalytic oxidation efficiency. Regarding the infrared surface temperature (**Figure 10(b)**), all samples exhibited a specific trend: the temperature initially increased and then decreased with rising air flow. This phenomenon is attributed to reduced heat retention in the combustion zone at higher flow velocities. Specifically, PTSY-11-NFAs attained a peak temperature of 587˚C at 0.8 L/min, surpassing that of PTSY-8-NFAs (566˚C) by 21˚C. This rapid attainment of peak temperature corroborates the superior catalytic activity and efficient heat generation of PTSY-11-NFAs, aligning well with the enhanced redox performance revealed by the H2-TPR analysis.

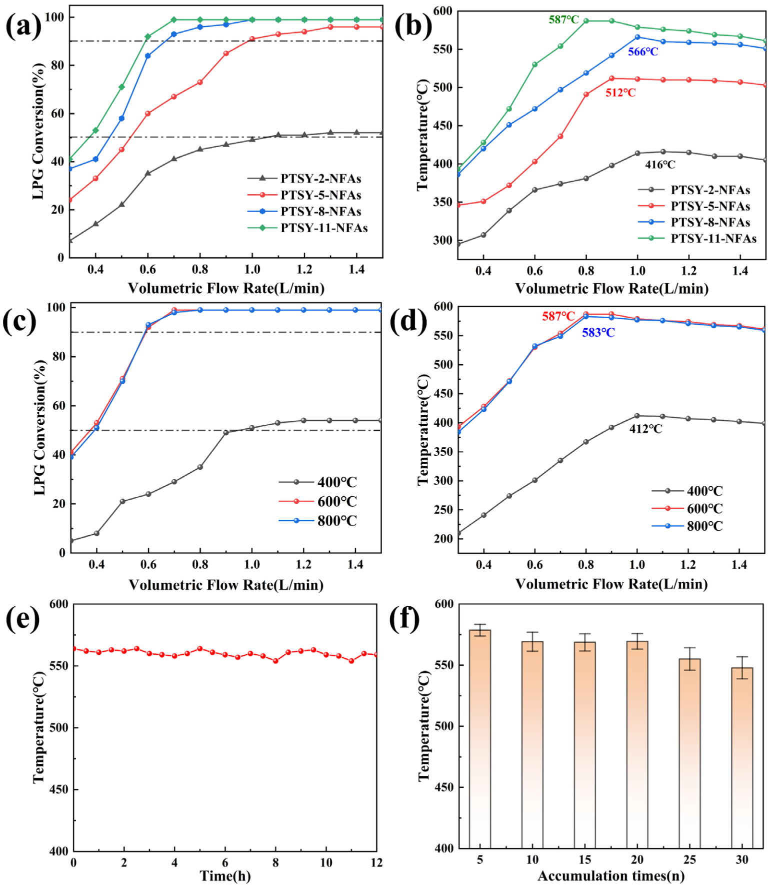

**Figure 10.** (a) Conversion rates of LPG and (b) infrared temperatures of catalytic combustion for PTSY-2-NFAs, PTSY-5-NFAs, PTSY-8-NFAs, and PTSY-11-NFAs under different air flow rates; Effects of calcination temperature on (c) conversion rates of LPG and (d) infrared temperatures of catalytic combustion for PTSY-11-NFAs under different air flow rates; (e) Stability of continuous catalytic combustion for PTSY-11-NFAs; (f) Test results of reusability for PTSY-11-NFAs.

The impact of calcination temperature on the catalytic performance of PTSY-11-NFAs was examined under varying air flow rates (**Figure 10(c)** and **Figure 10(d)**). With the 0.3 - 0.7 L/min range, both LPG conversion and infrared temperature increased with the air flow rate for all samples. The catalyst calcined at 400˚C exhibited inferior performance. This is attributed to the incomplete decomposition of organic precursors. The resulting residual carbonaceous species block active sites, thereby limiting catalytic efficiency. Conversely, samples calcined at 600˚C and 800˚C achieved LPG conversions exceeding 95% and surface temperatures above 550˚C. These metrics indicate superior redox capability and enhanced surface activation. Consequently, elevated calcination temperatures promote structural stabilization and strengthen metal-support interactions without compromising catalytic activity. This improves the thermal tolerance of PTSY-11-NFAs for sustained infrared combustion.

Balancing experimental safety and energy efficiency, the PTSY-11-NFA sample calcined at 600˚C was selected for stability and durability assessment. The tests were conducted at an air flow rate of 0.8 L/min. As depicted in **Figure 10(e)**, the infrared surface temperature remained stable at approximately 560˚C throughout 12 h of continuous operation. Notably, negligible fluctuation was observed during this period. Subsequently, the catalyst underwent 30 consecutive reuse cycles, with each cycle lasting 12 h (**Figure 10(f)**). Even after this rigorous testing, the infrared temperature showed only a modest decline of 50˚C from its initial value. These results demonstrate that the PTSY-11-NFA catalyst possesses robust thermal stability and excellent reusability under practical combustion conditions.

## 3.3. Evaluation of Catalytic Infrared Heater for Catalyst

### 3.3.1. Assessment of Commercially Available Catalyst and PTSY-11-NFAs Catalyst

To assess its practical efficacy, the high-performing PTSY-11-NFA catalyst was compared with a commercial catalyst (**Figure 11**). As shown in **Figure 11(a)**, PTSY-11-NFAs achieved over 90% LPG conversion at a relatively low air flow rate of 0.6 L/min. In contrast, the commercial catalyst required a higher flow rate of 1.0 L/min to achieve a similar conversion level. Additionally, in terms of thermal output (**Figure 11(b)**), PTSY-11-NFAs reached a peak infrared temperature of 587˚C at 0.8 L/min, exceeding the commercial catalyst's temperature of 568˚C by 19˚C. These comparative findings underscore the superior catalytic efficiency and heat generation of PTSY-11-NFAs. This performance advantage is attributed to its optimised nanofibrous architecture and highly dispersed Pd active sites.

### 3.3.2. Temperature Distribution of Catalytic Infrared Heater

**Figure 12(a)** illustrates the configuration of temperature measurement points on the catalytic infrared heater. During the test, LPG was injected at point 8 and diffused uniformly across the surface, facilitating stable and homogeneous infrared combustion. **Figure 12(b)** presents the corresponding 3D temperature profile. Notably, a high-temperature region covered approximately 90% of the surface, where temperatures exceeded 475˚C. The overall surface temperatures ranged from a minimum of 423˚C to a peak of 509˚C. The slight temperature drop observed at the periphery was ascribed to incomplete catalyst packing and mechanical constraints from edge riveting. These factors locally restricted gas flow and oxidation. Despite these minor edge effects, the heater exhibited exceptional thermal uniformity and operational stability. This validated the significant potential of nanofibrous aerogel catalysts for advanced infrared heating applications.

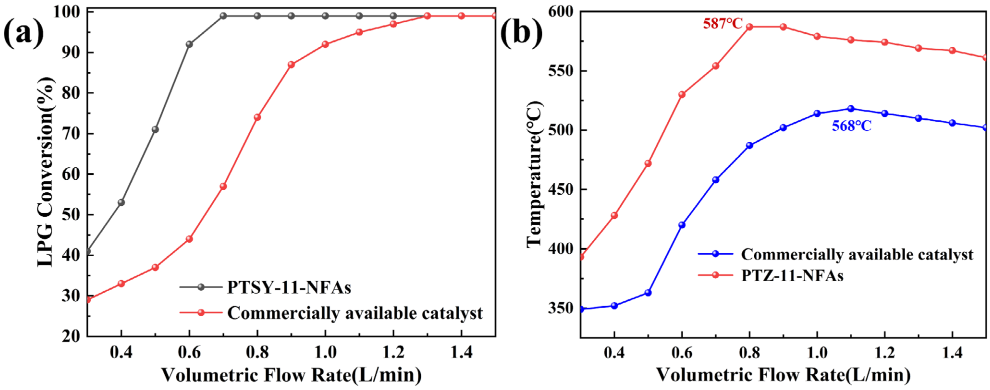

**Figure 11.** (a) Conversion rates of LPG, (b) Infrared temperatures during catalytic combustion of PTSY-11-NFAs and commercially available catalysts under different air flow rates.

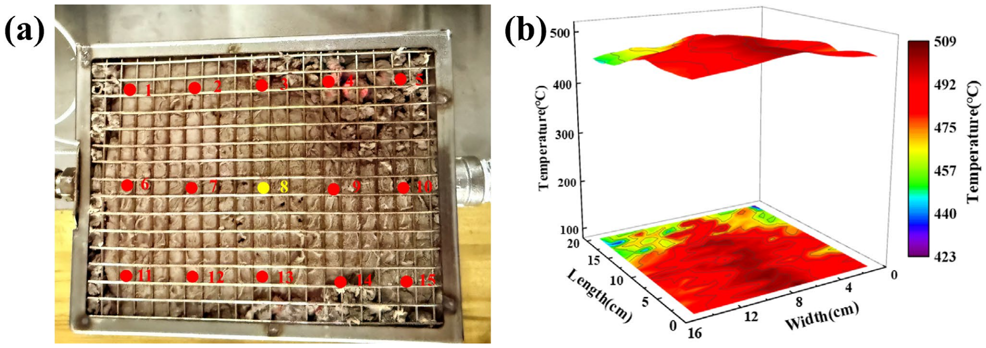

**Figure 12.** (a) Temperature distribution measurement points of the catalytic infrared heater; (b) Temperature distribution diagram of the catalytic infrared heater.

## 4. Conclusion

In this study, Pd-doped $TiO_2/SiO_2/Y_2O_3$ nanofibrous aerogel catalysts were developed via a one-step 3D electrospinning technique. This approach yielded a binder-free, continuously interconnected porous framework, wherein $Y_2O_3$ played a pivotal role in stabilizing the nanofibrous architecture. Furthermore, the incorporation of Pd optimized the crystalline structure and pore characteristics, thereby facilitating gas diffusion and efficient LPG oxidation. The resulting aerogels demonstrated exceptional thermal stability and mechanical resilience, retaining over 90% elastic recovery after 40 compression cycles. Among the prepared series, the optimized PTSY-11-NFA catalyst achieved an LPG conversion efficiency of 99% and a peak infrared surface temperature of 587˚C. A prototype infrared heater integrated with this catalyst displayed a highly uniform temperature distribution, surpassing the performance of a commercial benchmark. These findings provide a scalable and reliable strategy for constructing 3D nanofibrous aerogels and highlight their significant potential for advanced catalytic infrared heating applications.

## Funding

Jiangsu Modern Agricultural Machinery Equipment and Technology Promotion Project (NJ205-16).

## Conflicts of Interest

The authors assert that there are no conflicts of interest about the publishing of this work.

## References

[1] Qin, M., Chew, B.T., Yau, Y.H., Wang, X., Wang, C., Luo, X., *et al.* (2023) Emergency Heater Based on Gas-Fired Catalytic Combustion Infrared Technology: Structure, Evaluation and Thermal Response. *Energy*, **274**, Article ID: 127426. https://doi.org/10.1016/j.energy.2023.127426

[2] Jiaqiang, E., Luo, B., Han, D., Chen, J., Liao, G., Zhang, F. and Ding, J. (2022) A Comprehensive Review on Performance Improvement of Micro Energy Mechanical System: Heat Transfer, Micro Combustion and Energy Conversion. *Energy*, **239**, Article ID: 122509. https://doi.org/10.1016/j.energy.2021.122509

[3] Rumminger, M.D., Hamlin, R.D. and Dibble, R.W. (1999) Numerical Analysis of a Catalytic Radiant Burner: Effect of Catalyst on Radiant Efficiency and Operability. *Catalysis Today*, **47**, 253-262. https://doi.org/10.1016/s0920-5861(98)00306-x

[4] Bei, X., Yu, X., Li, D., Sun, Q., Yu, Y., Wang, Y., *et al.* (2023) Heat Source Replacement Strategy Using Catalytic Infrared: A Future for Energy Saving Drying of Fruits and Vegetables. *Journal of Food Science*, **88**, 4827-4839. https://doi.org/10.1111/1750-3841.16834

[5] Wang, T., Xia, L., Ni, M., Pan, S. and Luo, C. (2024) Fundamentals of Infrared Heating and Their Application in Thermosetting Polymer Curing: A Review. *Coatings*, **14**, Article 875. https://doi.org/10.3390/coatings14070875

[6] Ebrahimpour, V. and Esmailpour, K. (2024) Simultaneous Use of Convection and Radiation Heat Transfer for Iranian Pistachio Drying Using Catalytic Heater—Numerical and Experimental Study. *Frontiers in Mechanical Engineering*, **10**, Article 1459806. https://doi.org/10.3389/fmech.2024.1459806

[7] Hayes, R.E., Profic-Paczkowska, J., Jędrzejczyk, R. and Mmbaga, J.P. (2025) Catalytic Combustion of Fugitive Methane: Challenges and Current State of the Technology. *Applied Sciences*, **15**, Article 10269. https://doi.org/10.3390/app151810269

[8] Jodeiri, N., Mmbaga, J.P., Wu, L., Wanke, S.E. and Hayes, R.E. (2012) Modelling a Counter-Diffusive Reactor for Methane Combustion. *Computers & Chemical Engineering*, **39**, 47-56. https://doi.org/10.1016/j.compchemeng.2011.12.009

[9] Wu, B., Ma, Y., Guo, Y., Zielinska, M., Gao, K., Song, C., *et al.* (2024) Research Progress in the Application of Catalytic Infrared Technology in Fruit and Vegetable Processing. *Comprehensive Reviews in Food Science and Food Safety*, **23**, e13291. https://doi.org/10.1111/1541-4337.13291

[10] Liao, H., Zuo, P. and Liu, M. (2016) Study on the Correlation between the Surface Active Species of Pd/Cordierite Monolithic Catalyst and Its Catalytic Activity. *Materials Science and Engineering*: *B*, **211**, 45-52. https://doi.org/10.1016/j.mseb.2016.04.015

[11] Yang, Y., Wang, G., Yang, M., Yang, H., Liu, M. and Dang, F. (2021) Pt Modulates the Electronic Structure of Pd to Improve the Performance of Pd-Based Catalytic Combustion Catalyst. *International Journal of Hydrogen Energy*, **46**, 18391-18400. https://doi.org/10.1016/j.ijhydene.2021.03.028

[12] Pi, D., Li, W.Z., Lin, Q.Z., Huang, Q.F., Hu, H.Q. and Shao, C.Y. (2016) Highly Active and Thermally Stable Supported Pd@$SiO_2$ Core-Shell Catalyst for Catalytic Methane Combustion. *Energy Technology*, **4**, 943-949. https://doi.org/10.1002/ente.201600006

[13] Na, H., Zhu, T., Liu, Z. and Sun, Y. (2013) Promoting Effect of Zr on the Catalytic Combustion of Methane over Pd/$\gamma$-$Al_2O_3$ Catalyst. *Frontiers of Environmental Science & Engineering*, **8**, 659-665. https://doi.org/10.1007/s11783-013-0613-1

[14] Fessi, S., Ghorbel, A. and Rives, A. (2010) Sol-Gel Synthesis Combined with Solid ex-Change Method, a New Alternative Process to Prepare Improved Pd/$ZrO_2$-$Al_2O_3$-$SiO_2$ Catalysts. *Studies in Surface Science and Catalysis*, **175**, 797-800.

[15] Kucharczyk, B. (2011) Activity of Monolithic Pd/$Al_2O_3$ Catalysts in the Combustion of Mine Ventilation Air Methane. *PJCT*, **13**, 57-62. https://doi.org/10.2478/v10026-011-0050-5

[16] Xiao, W., Lu, L., Xu, Z., Huang, Y., Zhuang, Q., Qian, X., *et al.* (2025) A Superelastic Ceramic Aerogel for Flexible Pressure Sensor in Harsh Environment. *Composites Part B*: *Engineering*, **292**, Article ID: 112110. https://doi.org/10.1016/j.compositesb.2024.112110

[17] Cheng, X., Chang, X., Wu, F., Liao, Y., Pan, K., Fong, H., *et al.* (2024) Advanced Nanofabrication for Elastic Inorganic Aerogels. *Nano Research*, **17**, 8842-8862. https://doi.org/10.1007/s12274-023-6369-4

[18] Miao, J., Song, X., Xu, J., Xu, J., Duan, Z., Song, Y., *et al.* (2025) Ultralight, Elastic, Thermally Insulating, and High-Temperature Resistant $Al_2O_3$-$SiO_2$-$B_2O_3$ Nanofibrous Aerogels Prepared via the Direct Foaming Method. *ACS Applied Materials & Interfaces*, **17**, 12402-12414. https://doi.org/10.1021/acsami.4c20475

[19] Shao, W., Yue, W., Ren, L., Fan, G., Shi, P., He, J., *et al.* (2025) $Al_2O_3$/$SiO_2$ Sponges with a Three-Dimensional Lamellar Structure Based on Solution Blow Spinning for Superior Thermal Insulation and High Temperature Filtration. *Separation and Purification Technology*, **376**, Article ID: 134088. https://doi.org/10.1016/j.seppur.2025.134088

[20] Asadi-Pakdel, K., Mehdinavaz Aghdam, R., Shahedi Asl, M. and Faghihi Sani, M.A. (2020) Synthesis and Morphology Optimization of Electrospun SiBNC Nanofibers. *Ceramics International*, **46**, 6052-6059. https://doi.org/10.1016/j.ceramint.2019.11.063

[21] Wu, H., Pan, W., Lin, D. and Li, H. (2012) Electrospinning of Ceramic Nanofibers: Fabrication, Assembly and Applications. *Journal of Advanced Ceramics*, **1**, 2-23. https://doi.org/10.1007/s40145-012-0002-4

[22] Zhang, X., Wang, F., Dou, L., Cheng, X., Si, Y., Yu, J., *et al.* (2020) Ultrastrong, Superelastic, and Lamellar Multiarch Structured $ZrO_2$-$Al_2O_3$ Nanofibrous Aerogels with High-Temperature Resistance over 1300°C. *ACS Nano*, **14**, 15616-15625. https://doi.org/10.1021/acsnano.0c06423

[23] Zhang, X., Cheng, X., Si, Y., Yu, J. and Ding, B. (2022) Elastic and Highly Fatigue Resistant $ZrO_2$-$SiO_2$ Nanofibrous Aerogel with Low Energy Dissipation for Thermal Insulation. *Chemical Engineering Journal*, **433**, Article ID: 133628. https://doi.org/10.1016/j.cej.2021.133628

[24] Dou, L., Zhang, X., Shan, H., Cheng, X., Si, Y., Yu, J., *et al.* (2020) Interweaved Cellular Structured Ceramic Nanofibrous Aerogels with Superior Bendability and Compressibility. *Advanced Functional Materials*, **30**, Article ID: 2005928. https://doi.org/10.1002/adfm.202005928

[25] Zhang, M., Wang, Y., Zhang, Y., Song, J., Si, Y., Yan, J., *et al.* (2020) Conductive and Elastic $TiO_2$ Nanofibrous Aerogels: A New Concept toward Self-Supported Electrocatalysts with Superior Activity and Durability. *Angewandte Chemie International Edition*, **59**, 23252-23260. https://doi.org/10.1002/anie.202010110

[26] Dong, S., Maciejewska, B.M., Lißner, M., Thomson, D., Townsend, D., Millar, R., *et al.* (2023) Unveiling the Mechanism of the *in Situ* Formation of 3D Fiber Macroassemblies with Controlled Properties. *ACS Nano*, **17**, 6800-6810. https://doi.org/10.1021/acsnano.3c00289

[27] Vong, M., Diaz Sanchez, F.J., Keirouz, A., Nuansing, W. and Radacsi, N. (2021) Ultrafast Fabrication of Nanofiber-Based 3D Macrostructures by 3D Electrospinning. *Materials & Design*, **208**, Article ID: 109916. https://doi.org/10.1016/j.matdes.2021.109916

[28] Dong, S., Maciejewska, B., Millar, R. and Grobert, N. (2023) 3D Electrospinning of $Al_2O_3$/$ZrO_2$ Fibrous Aerogels for Multipurpose Thermal Insulation. *Advanced Composites and Hybrid Materials*, **6**, Article No. 186. https://doi.org/10.1007/s42114-023-00760-y

[29] Zhang, X., Liu, Y., Guo, X., Zhang, X., Jin, G., Li, C., *et al.* (2025) Manipulating Polymerization Degree and Charge Density to Achieve Self-Templated Electrospinning Superelastic Silica Curly Nanofibrous Aerogels for Thermal Insulation. *Ceramics International*, **51**, 38571-38578. https://doi.org/10.1016/j.ceramint.2025.06.094

[30] Tian, W., Tang, J., Zhang, M., Chang, M., Chen, X., Sun, J., *et al.* (2026) Three-dimensional Electrospinning and Catalytic Graphitization Directly Prepared High Flexibility, Elasticity and Graphitization Interwoven Crimp Micro/Nano-Carbon-Fibrous Aerogels. *Carbon*, **246**, Article ID: 120871. https://doi.org/10.1016/j.carbon.2025.120871

[31] Ali, S., Al-Marri, M.J., Al-Jaber, A.S., Abdelmoneim, A.G. and Khader, M.M. (2018) Synthesis, Characterization and Performance of Pd-Based Core-Shell Methane Oxidation Nano-Catalysts. *Journal of Natural Gas Science and Engineering*, **55**, 625-633. https://doi.org/10.1016/j.jngse.2018.01.023

[32] Fu, J., Cao, S., Yu, J., Low, J. and Lei, Y. (2014) Enhanced Photocatalytic $CO_2$-Reduction Activity of Electrospun Mesoporous $TiO_2$ Nanofibers by Solvothermal Treatment. *Dalton Transactions*, **43**, 9158-9165. https://doi.org/10.1039/c4dt00181h

[33] Wang, H., Li, W., Wang, J., Chang, H., Jameel, H., Zhang, Q., *et al.* (2017) A Ternary Composite Oxides $S_2O_8^{2-}$/$ZrO_2$-$TiO_2$-$SiO_2$ as an Efficient Solid Super Acid Catalyst for Depolymerization of Lignin. *RSC Adv.*, **7**, 50027-50034. https://doi.org/10.1039/c7ra09489b

[34] Zangeneh, H., Zinatizadeh, A.A., Zinadini, S., Feyzi, M. and Bahnemann, D.W. (2019) Preparation and Characterization of a Novel Photocatalytic Self-Cleaning PES Nanofiltration Membrane by Embedding a Visible-Driven Photocatalyst Boron Doped-$TiO_2SiO_2$/$CoFe_2O_4$ Nanoparticles. *Separation and Purification Technology*, **209**, 764-775. https://doi.org/10.1016/j.seppur.2018.09.030

[35] Khung, Y.L., Rusli, S. and Hsiao, Y. (2022) Thermal Grafting of Aniline Derivatives to Silicon (1 1 1) Hydride Surfaces. *Applied Surface Science*, **580**, Article ID: 152257. https://doi.org/10.1016/j.apsusc.2021.152257

[36] Zhu, F., Wen, J., Guo, H., An, J., Wang, G., Ren, G., *et al.* (2023) Low-temperature Catalytic Performance Improvement of Ru/$TiO_2${001} for *O*-Dichlorobenzene Oxidation. *Chemical Engineering Journal*, **473**, Article ID: 145186. https://doi.org/10.1016/j.cej.2023.145186

[37] Bi, W., Wu, Y., Chen, C., Zhou, D., Song, Z., Li, D., *et al.* (2020) Dye Sensitization and Local Surface Plasmon Resonance-Enhanced Upconversion Luminescence for Efficient Perovskite Solar Cells. *ACS Applied Materials & Interfaces*, **12**, 24737-24746. https://doi.org/10.1021/acsami.0c04258

[38] Wang, C., Tang, Y., Geng, Z., Guo, Y., Tan, X., Hu, Z., *et al.* (2023) Modulating Charge Accumulation via Electron Interaction for Photocatalytic Hydrogen Evolution: A Case of Fabricating Palladium Sites on $ZnIn_2S_4$ Nanosheets. *ACS Catalysis*, **13**, 11687-11696. https://doi.org/10.1021/acscatal.3c02563

[39] Xu, Z., Jiang, J., Wang, M., Wang, J., Tang, Y., Li, S., *et al.* (2023) Enhanced Levofloxacin Degradation by Hierarchical Porous $Co_3O_4$ with Rich Oxygen Vacancies Activating Peroxymonosulfate: Performance and Mechanism. *Separation and Purification Technology*, **304**, Article ID: 122055. https://doi.org/10.1016/j.seppur.2022.122055

[40] Hao, C., Zhao, Y., Zhou, Y., Zhou, L., Xu, Y., Wang, D., *et al.* (2007) Interactions between Metal Chlorides and Poly(Vinyl Pyrrolidone) in Concentrated Solutionsand Solid-State Films. *Journal of Polymer Science Part B*: *Polymer Physics*, **45**, 1589-1598. https://doi.org/10.1002/polb.21138

[41] Ren, Y., Zhang, B., Ye, J., Zhang, H., Zhong, Z., Wang, Y., *et al.* (2023) Design and Preparation of Novel $Y_2O_3$-$SiO_2$ Composite Aerogels for High-Temperature Thermal Insulators. *Journal of Non-Crystalline Solids*, **605**, Article ID: 122177. https://doi.org/10.1016/j.jnoncrysol.2023.122177

[42] Letichevsky, S., Zonetti, P.C., Reis, P.P.P., Celnik, J., Rabello, C.R.K., Gaspar, A.B., *et al.* (2015) The Role of M-$ZrO_2$ in the Selective Oxidation of Ethanol to Acetic Acid Employing PdO/m-$ZrO_2$. *Journal of Molecular Catalysis A*: *Chemical*, **410**, 177-183. https://doi.org/10.1016/j.molcata.2015.09.012

[43] Schwartz, W.R. and Pfefferle, L.D. (2012) Combustion of Methane over Palladium-Based Catalysts: Support Interactions. *The Journal of Physical Chemistry C*, **116**, 8571-8578. https://doi.org/10.1021/jp2119668